Materials Advances

ROYAL SOCIETY OF CHEMISTRY

PAPER

View Article Online
View Journal | View Issue

Cite this: *Mater. Adv.*, 2025, **6**, 1403

Exploring the effects of zirconium doping on barium titanate ceramics: structural, electrical, and optical properties

Suravi Islam, *[a] Mohammad Robel Molla,[a] Nazia Khatun,[a] Nazmul Islam Tanvir,[a] Mahmuda Hakim[b] and Md. Saidul Islam[a]

Received 24th September 2024,
Accepted 7th January 2025

DOI: 10.1039/d4ma00967c

rsc.li/materials-advances

In this study, polycrystalline $BaZr_xTi_{1-x}O_3$ (x = 0.00, 0.05, 0.10, 0.15, and 0.20) ceramics were synthesized through a solid-state reaction technique. The effect of zirconium doping on the properties of barium titanate ($BaTiO_3$) was investigated by various characterization tools. The structural and morphological properties of the synthesized materials were studied by X-ray diffraction (XRD), Raman spectroscopy, and field emission scanning electron microscopy (FE-SEM). The electrical properties of the Zr-doped $BaTiO_3$ (BZT) materials were examined by impedance spectroscopy and the optical properties were investigated using UV-Vis-NIR spectroscopy. The XRD analyses of the prepared BZT materials revealed a single-phase tetragonal structure. The inclusion of Zr^{4+} in the BT matrix did not significantly affect the Raman-active modes, suggesting that the tetragonal crystal structure was retained in the as-synthesized samples. FE-SEM analyses revealed that the grain size initially increased from 49.36 nm to 53.24 nm for x = 0.05 wt% and then decreased gradually for higher concentrations up to x = 0.15 wt% (26.99 nm). The dielectric constant, dielectric loss, conductivity, and quality factor determined from the impedance data demonstrated that Zr^{4+} addition significantly influenced the electrical properties of BT. The band gap energy, E_g, of the synthesized samples were found in the range of 3.19–3.37 eV, which was calculated from the diffuse reflection data. The experimental results suggest that the BZT ceramic materials are suitable for energy storage device applications.

1. Introduction

Fabrication of lead (Pb)-free ceramic materials has attracted increasing attention from researchers over the last few decades. A lot of research is being conducted on lead-based ceramic materials for energy storage, piezoelectric actuators, ferroelectric random access memory, *etc.* owing to their outstanding performances.[1,2] However, Pb-constituted materials are toxic and harmful to the environment. Barium titanate ($BaTiO_3$, BT) is an excellent ferroelectric, dielectric, and piezoelectric material,[3] which has numerous applications in multilayer ceramic capacitors (MLCCs), thermistors, transducers, thermal sensors, medical diagnostic transducers, and electroluminescent panels.[4] Perovskite-type oxide materials are generally expressed as ABO_3, among which BT has attracted great attention as a model perovskite material.[5] BT can be synthesized by various routes, such as sol–gel synthesis,[6] direct synthesis,[7] hydrothermal synthesis,[8] solid-state synthesis,[9] and a sonochemical process.[10] Among other methods, high-energy ball-milling is a well-known affordable, eco-friendly, and convenient technique for the preparation of BT powders from low-cost raw substances. Since BT ceramics are traditionally obtained *via* sintering, they does not cover all the requirements for very thin dielectric layers owing to their irregular grain size and morphology, imperfect homogeneity and dispersion.[11] Developing high-quality nano-sized BT materials, which are free of by-products, is still a challenging task for researchers.[4] The electrical properties of BT ceramics can be increased by introducing rare earth metals, which are actually amphoteric dopants occupying two sites, A and B, following an A/B ratio, where oxygen is incorporated in the structure.[12] It has been reported that doping a metal at the A and B sites leads to them acting as donors and acceptors, respectively, which can enhance or reduce the reliability of various devices.[13] Kim reported that rare earth metals can dominantly and easily erect better shell and core–shell structures when they are inserted as dopants in to BT.[14] Typically, the A site (Ba^{2+}) of BT is normally substituted by Sr^{2+}, Ca^{2+}, Mg^{2+}, *etc.*[15–18] while the B site (Ti^{4+}) is

[a] *Industrial Physics Division, BCSIR Dhaka Laboratories, Bangladesh Council of Scientific and Industrial Research (BCSIR), Dhaka 1205, Bangladesh. E-mail: suravii@yahoo.com, suraviislambcsir@gmail.com*
[b] *Biomedical and Toxicology Research Institute (BTRI), BCSIR, Dhaka 1205, Bangladesh*

commonly substituted by Zr^{4+}, Sn^{4+}, Nb^{5+}, *etc.*[15,17] The ionic radius of chemically stable Zr^{4+} (0.72 Å) is comparatively larger than that of Ti^{4+} (0.605 Å), prompting zirconium to easily expand inside the lattice configuration[18] and facilitating the substitution of Ti^{4+} by Zr^{4+}. Our current research was focused on the solid-state synthesis of BT, the impacts of zirconium doping on BT, and investigation of the structural, electrical, and optical properties of the synthesized materials. In ceramics materials, rare earth elements have been shown to have significant stabilizing effects on the temperature dependence of the relative dielectric constant and lower dissipation capabilities of ceramics.[5] Since BZT has less dielectric loss along with a larger dielectric non-linearity than Sr-doped BT, we chose the Z element to improve the dielectric performance of BT materials.

There are many reports on Zr-doped $BaTiO_3$, and most of these articles highlighted the dielectric temperature dependence.[1,15,17] However, frequency-dependent dielectric studies, and the piezoelectric properties and optical properties of BZT have received less attention. Consequently, we paid special attention to the analysis of these properties for our synthesized samples. Our present study reports the synthesis of BT and Zr-doped BT with different compositions of Zr and starting constituents, which were pre-activated by ball-milling to obtain fine and by-product-free BT. The structural transformation from tetragonal to cubic, ferroelectric to paraelectric phase transformation, dielectric loss factor, dielectric constant, and bandgap energy were examined at different concentrations of Zr-doped BT ceramics, and the findings show that they may be suitable for optoelectronic devices.

2. Experimental

2.1. Materials and method

Barium carbonate; $BaCO_3$ (CAS no. 513-77-9, 99% purity, China), titanium oxide; TiO_2 (CAS no. 13463-67-7, 99% purity, Sigma-Aldrich, Germany), zirconium oxide; ZrO_2 (CAS no. 1314-23-4, 99% purity, BDH, UK), and polyvinyl alcohol (CAS no. 9002-89-5, 98% purity, BDH, UK) were utilized without further purification. Pure and zirconium-doped barium titanate ($BaTi_{1-x}Zr_xO_3$; x = 0.00, 0.05, 0.10, 0.15, and 0.20) BT ceramic materials were developed through a solid-state reaction method utilizing a high-energy planetary ball-mill. Initially, three starting materials, namely barium carbonate, titanium oxide, and zirconium oxide, were pre-activated by ball-milling for 4 h at 150 rpm and room temperature. After pre-activation, the raw powders were weighed in certain proportions in line with the above-mentioned chemical formula, in which the ball (10 nm diameter) to powder weight ratio was 2 : 1. The measured samples were mixed thoroughly and ball-milled for 4 h at a fixed 150 rpm, at room temperature. Then, the powder samples were pre-sintered at 700 °C for 3 h and milled for 30 min by hand. Subsequently, 4% polyvinyl alcohol aqueous solution was blended with the samples as a binder to form pellets. Specifically, they were pressed into disk-like pellets by applying a pressure of 2 ± 0.5 MPa for 1 min. Finally, the pellets were sintered at 1300 °C for 3 h in the air in a programmable muffle furnace (Nabertherm, Germany).

2.2. Characterization

The synthesized samples BT and Zr-doped BT (BZT) were investigated by different characterization techniques. For structural analysis, X-ray diffraction (XRD) (Rigaku Smart Lab, Japan), with Cu-Kα radiation (λ = 1.5406 Å), a scanning rate of 10° min^{-1}, 40 kV power at 40 mA, and 0.02° steps, was used to confirm the crystallinity of the synthesized samples at room temperature. The optical properties were observed using an ultraviolet-visible-near-infrared (UV-vis-NIR) spectrophotometer (UV-2600, Shimadzu, Japan) with a wavelength range of 220–1400 nm. Field emission scanning electron microscope (FE-SEM) was performed on a JSM-7610F system (Japan). Also, energy-dispersive X-ray spectroscopy (EDX) was utilized to analyze the surface morphology and identify the elemental compositions of the BT and Zr-doped BT materials. The average grain sizes of the synthesized samples were explored using the linear intercept method. ImageJ and Origin Pro software were used to attain the grain-size distribution. Raman spectroscopy (Macro RAM, Japan) was used for studying the structural fingerprints. The piezoelectric constant, d_{33}, was determined using a quasi-static piezoelectric constant testing meter (ZJ-3A, China). Silver paste (D. Leipziger Str. 10, Germany) was painted as a conductive layer on the surface of the pellet samples to be used as electrodes for measuring the dielectric properties. Impedance analysis (Agilent 4294A, 40 kHz to 120 MHz) was used to determine the electrical parameters.

3. Results and discussion

3.1. Structural properties

X-Ray diffraction (XRD) analysis was conducted to derive the crystallinity and phase purity of the zirconium-doped BT ($BaZr_xTi_{1-x}O_3$) at different doping concentrations, *i.e.*, at x = 0.00, 0.05, 0.10, 0.15, and 0.20. The XRD patterns of the pure and doped barium titanate ceramics obtained between scan angles of 20° and 80° at room temperature are shown in Fig. 1. These reveal that all the samples were crystallized into a single-phase perovskite structure with the tetragonal space group (*P*4*mm*) made by one molecule per unit cell. Moreover, the pattern of the synthesized samples well-matched JCPDS card no. # 05-0626 showing they followed a phase structure of the typical perovskite (ABO_3), and indicating Zr^{4+} had diffused successfully into the lattice of the $BaTiO_3$ matrix to form a stable solid solution. Moreover, Zr-doped BT can have tetragonal, rhombohedral, or an orthorhombic structure at room temperature dependent on the concentration of Zr, as reported in earlier studies.[19,20]

The diffraction peaks observed at 2θ = 22.22°, 31.48°, 38.88°, 45.36°/44.88°, 50.97°, 56.25°, and 65.73° corresponding to the Bragg reflection planes (100), (110), (111), (002)/(200), (210), (211), (220), respectively, matched with those previously reported.[20,21]

The lattice parameters were calculated using the following equation:

$$\frac{1}{d^2} = \frac{(h^2 + k^2)}{a^2} + \frac{l^2}{c^2}$$

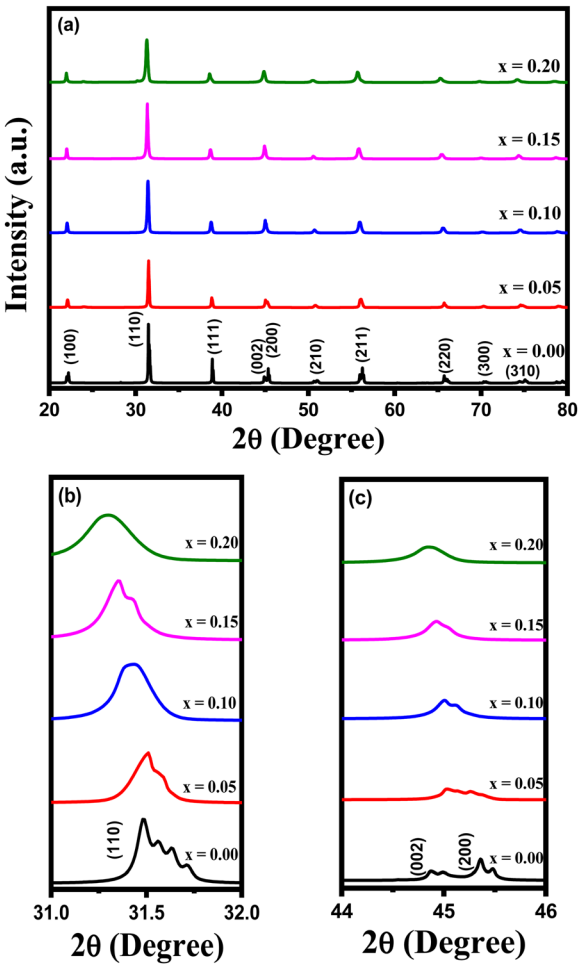

Fig. 1 (a) XRD patterns of $BaZr_xTi_{1-x}O_3$ (x = 0.00, 0.05, 0.10, 0.15, and 0.20), (b) magnified pattern of the (110) peaks around 2θ = 31°, and (c) (002) (200) peaks illustrating a shift at around 2θ = 45° for various x contents.

where d denotes the interplanar spacing, and h, k, and l are the Miller indices noted from the JPDS card and based on a tetragonal symmetry.

The average crystalline sizes (t) of the samples were measured for the (002) and (200) reflections using the Debye–Scherrer equation,[22] as follows:

$$t = \frac{0.9\lambda}{\beta \cos\theta}$$

where λ is the X-ray wavelength (λ = 1.540562 Å), θ denotes the Bragg's diffraction angle, and β is the full width at half maximum. Accordingly, the lattice parameters a, b, c, and the tetragonality, c/a, and crystallite size were determined and are presented in Table 1. The calculated value of the crystal size at x = 0.00 was 45.80 nm, while the range of crystal sizes from x = 0.05 to x = 0.20 was 22.68–33.24 nm, and the lattice parameter c was 4.037. Furthermore, according to Fig. 1(a) and the prior literature,[22–25] the data clearly indicated the formation of tetragonal BZT for each concentration, except for x = 0.15 and x = 0.20, which demonstrated pseudo-cubic structured without any secondary phase. The trend of increased cell volume with enhancing Zr concentration (x = 0.05 to 0.20), indicates the incorporation of Zr^{4+} in the core side of lattice structure and completed the B-site replacement, up to a certain penetration in BT elements which leads to a slacken tetragonality.[20]

The magnified XRD pattern at around 2θ = 31° in Fig. 1(b) shows that the (110) peaks were shifted to lower theta values with the higher concentration of zirconium doping. In Fig. 1(c), the splitting of a certain peak into (002) and (200) planes at around 45° provides strong indication of the tetragonal structure of pure BT.[22] The peaks were shifted to lower angles with increasing the Zr content and showed the transformation from the tetragonal phase to the cubic phase.[21]

The lattice parameters a and c of tetragonal BT increased with the Zr doping, owing to the substitution of the smaller Ti^{4+} (radius = 0.605 Å) by the larger radius (0.72 Å) Zr^{4+}. Therefore, the Zr atom's ionic and atomic sizes are greater than those of titanium atoms due to its electronic configuration and electron cloud density. The interplanar spacing of the crystal may be increased with the increment in the lattice parameters, so there would be a rise in the unit cell volume.[22] Indeed, the unit cell volume increased with the rise in the content of Zr because of the increase in the lattice parameters, and hence θ (the angle) decreased. Consequently, a shift towards lower 2θ was obtained for the most intense peak, as illustrated in Fig. 1(b), which also matched with the findings reported in ref. 22. In Fig. 1(c), it can be inferred that the (002) peak tended to shrink as the zirconium concentration rose, which increased the tetragonality since Ti^{4+} has a smaller radius than Zr^{4+}.

Fig. 1(a)–(c) demonstrate that, as the Zr^{4+} concentration increased, the lattice parameter (a) increased linearly in accordance with Vegard's law, while the lattice parameter (c) increased through a different trend. In addition, the tetragonal symmetry (c/a) was >1 for all the samples, indicating that the elongation of the (TiO_6) octahedron occurred along the Z-axis, where the symmetry remained the same.[11,12] The XRD patterns analysis indicated that the splitting in the (001) and (100) reflection declined with the increase in the Zr^{4+} ions content, indicating the steady phase transition from the tetragonal to pseudo-cubic structure. This effect also agreed with the report of Yao *et al.*, where, beside XRD confirmation, it was also confirmed from the Raman spectra; whereby the Raman intensity of BZT decreased gradually and the peaks turned into weak and wider, revealing that there was a slight structural reordering, like phase transition from tetragonal to cubic.[6] Furthermore, it is evident from Table 1 that the crystallite size showed a decreasing trend with increasing the Zr^{4+} ions content.

The Williamson–Hall method was utilized to calculate the crystallite sizes (D) of the samples, also considering the X-ray diffraction peak widening β_{hkl} (FWHM), which can be given by the following:[23]

$$\beta_{hkl} = \beta_{size} + \beta_{strain}$$

This relation can be modified by

$$\beta_{hkl} = \frac{0.94\lambda}{D\cos\theta} + 4\epsilon \tan\theta$$

Table 1 Structural parameters of $BaZr_xTi_{1-x}O_3$, where x = 0.00, 0.05, 0.10, 0.15, and 0.20

Samples $BaZr_xTi_{1-x}O_3$	Lattice parameter "$a = b$" (Å)	Lattice parameter "c" (Å)	Tetragonality (c/a)	Cell volume V (Å^3)	Crystalline size, D (nm)		Strain, ε	
					Debye–Scherrer method	Williamson–Hall method	Debye–Scherrer method ($\times10^{-3}$)	Williamson–Hall method ($\times10^{-3}$)
$BaTiO_3$	3.9954	4.0359	1.0101	64.426	56.50	44.27	2.262	0.60
$BaZr_{0.05}Ti_{0.95}O_3$	4.0039	4.0224	1.0046	64.484	49.30	12.59	2.589	3.45
$BaZr_{0.10}Ti_{0.90}O_3$	4.0139	4.0241	1.0025	64.834	39.22	68.93	3.263	2.98
$BaZr_{0.15}Ti_{0.85}O_3$	4.0224	4.0309	1.0021	65.219	45.39	167.50	2.827	3.12
$BaZr_{0.20}Ti_{0.80}O_3$	4.03838	4.0376	0.9998	65.845	29.43	28.19	4.366	3.25

or,

$$\beta_{hkl}\cos\theta = \frac{0.94\lambda}{D} + 4\epsilon\sin\theta$$

or,

$$\beta_{hkl}\cos\theta = \epsilon(4\sin\theta) + \frac{0.94\lambda}{D}$$

where λ is the wavelength of Cu-Kα radiation, D is the crystallite size, β_{hkl} is the full width at half maximum, and ϵ denotes the micro-strain of the synthesized samples. The W–H plots of $\beta_{hkl}\cos\theta$ against $4\sin\theta$ for the BZT samples are demonstrated in Fig. 2. The average D and ϵ values were calculated based on the linear line's slope and y-intercept, and the results are summarized in Table 1. The crystallite size and micro-strain of all the synthesized samples followed the same pattern when compared to the Debye–Scherrer and W–H analyses,[24] and were associated with peak broadening. The Goldschmidt tolerance factor, t, is a geometrical factor that has received widespread acceptance to measure the formation of perovskite structures and indicates their stability. It extends the range of what is predicted to be appropriate for A site cations inside cavities.

The Goldschmidt's tolerance factor of the synthesized samples was measured conforming to the following general principle:[24]

$$t = \frac{(r_A + r_O)}{\sqrt{2}(r_B + r_O)}$$

where r_A, r_B, and r_O represent the ionic radii of A, B, and O oxygen ions, respectively, of the perovskite structure ABO_3. For BT ceramics, the tolerance factor t = 1.06 revealed a distortion of the crystal structure, where the ionic radii of r_A, r_B, and r_O were Ba^{2+} = 1.61, Ti^{4+} = 0.605, and O^{2-} = 1.4 Å, correspondingly. The introduction to ZrO_2 (the ionic radius of Zr^{4+} = 0.72 Å) into the BT lattice led to the decrease in the t value. The calculated tolerance factors of the $BaTi_{1-x}Zr_xO_3$ samples are reported in Table 2. Similar results for t values ranging from 1.073 to 1.063 were reported in ref. 22. Here, it is expected that the small ions Ti^{4+}, large ions Ba^{2+}, and intermediate Zr^{4+} ions would occupy the B sites, A sites, and both sites, respectively with various partitions for every ion. However, evaluation among ions occupying different sites based on tolerance factors is a qualitative parameter.

3.2. Raman analysis

Raman spectroscopy is a potent technique to elucidate the structural information and chemical fingerprint of a material. In order to gain clear insights into BT and doped BZT, we performed Raman analysis. Fig. 3 outlines the Raman spectra of $BaTi_{1-x}Zr_xO_3$ (x = 0.00, 0.05, 0.10, 0.15, and 0.20) sintered at

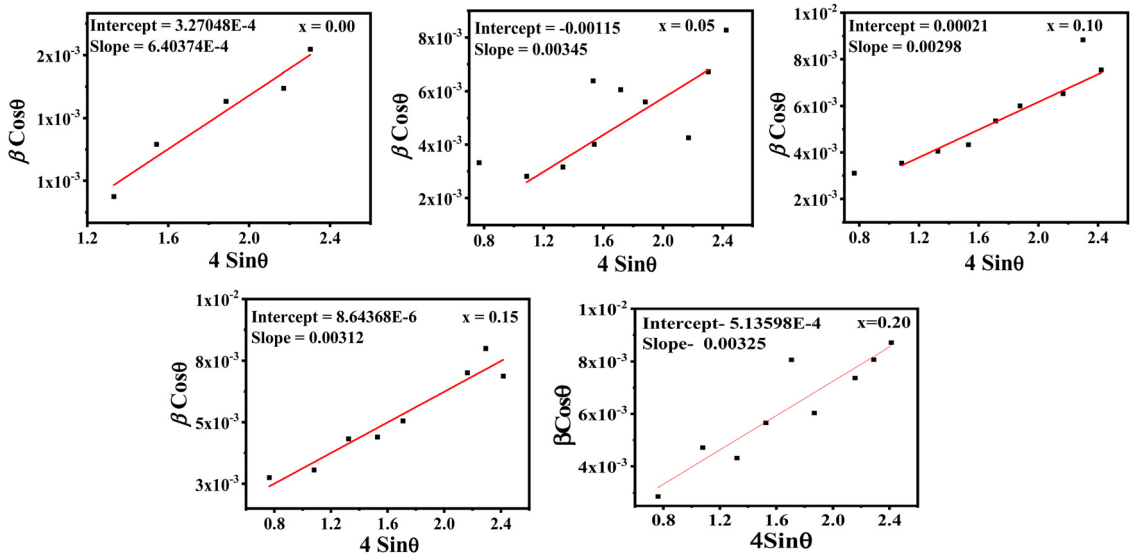

Fig. 2 Williamson–Hall plots of the $BaZr_xTi_{1-x}O_3$ ceramics for varied concentrations, x = 0.00, 0.05, 0.10, 0.15, and 0.20.

Table 2 Molecular weight, cell volume, tolerance factor (t), average grain size, and piezoelectric coefficient, d_{33}, of $BaZr_xTi_{1-x}O_3$ (where x = 0.00, 0.05, 0.10, 0.15, and 0.20)

Sample $BaZr_xTi_{1-x}O_3$	Molecular weight (g)	Cell volume (cm^3) $\times 10^{-23}$	Tolerance factor (t)	d-spacing (Å)	Average grain size (nm)	Piezoelectric coefficient, d_{33} (pC N^{-1})	Bandgap energy, E_g (eV)
x = 0.00	233.192	6.4426	1.0763	2.8396	383 ± 100	124	3.20
x = 0.05	235.360	6.4484	1.0731	2.8369	367 ± 114	174	3.19
x = 0.10	237.528	6.4834	1.0699	2.8477	220 ± 35	130	3.33
x = 0.15	239.696	6.5219	1.0667	2.8507	109 ± 58	139	3.32
x = 0.20	241.864	6.5845	1.0636	2.8587	425 ± 95	136	3.38

1300 °C for 3 h. Three remarkable peaks could be observed at 306 cm^{-1} [B_1, E (TO + LO)], 517 cm^{-1} [A_1 (TO), E (TO),] and 716 cm^{-1} [A1 (LO), E (LO)], indicating the formation of tetragonal BT.[26,27] BT has one molecule (5 atoms) per unit cell in both the paraelectric and ferroelectric phases, resulting in $12(3 \times 5 - 3)$ long-wavelength optical modes.

The optical modes changed in tandem with 3F1u + F2u during the paraelectric phase (*Pm3m* symmetry). Since the F1u modes in the paraelectric phase of BT were only infrared (IR) active and the F2u mode was mute, there was no Raman-active mode in this phase. Every F1u mode split into an A1 mode (nondegenerate) and an E mode (doubly degenerate) in the ferroelectric phase with the tetragonal structure (*P4mm* symmetry), while the F2u mode split into E and B1 modes. In addition, the B1 mode was exclusively Raman active, while the A1 and E modes were both Raman and infrared active. Furthermore, because of the long-range electrostatic interactions associated with lattice ionicity, the A1 and E optical modes further split into longitudinal (LO) and transverse (TO) modes.[27]

It was observed that above 716 cm^{-1}, the intensities of the peaks gradually declined with the enhancement of x ($x > 0.05$), indicating the phase transition from the quadratic to pseudo-cubic phase.[28] The peaks at 716 cm^{-1} were broadened gradually and shifted to lower λ as well. The band intensity at 306 cm^{-1} was reduced with increasing the doping percentage, and it was estimated that the replacement of Ti by Zr did not entirely destroy the long-range order of BT. Again, Raman shifts towards lower wavelength were observed for higher concentrations of Zr in BT. The small peak at 262 cm^{-1} [A_1 (TO), E (TO)] for x = 0.00 suggested the quadratic phase of BT.[29] No remarkable peak was observed at 195 cm^{-1} for pure BT, but for x = 0.05 and x = 0.20, sharp and broad peaks were detected, clearly demonstrating the impact of zirconium. This was also indicated by the formation of small crystals. Anti-resonance was observed by the characteristic band at ~306 cm^{-1} of ferroelectric BT, which suggested that the local structure of the BO_6 octahedron departed from a proper cubic symmetry.

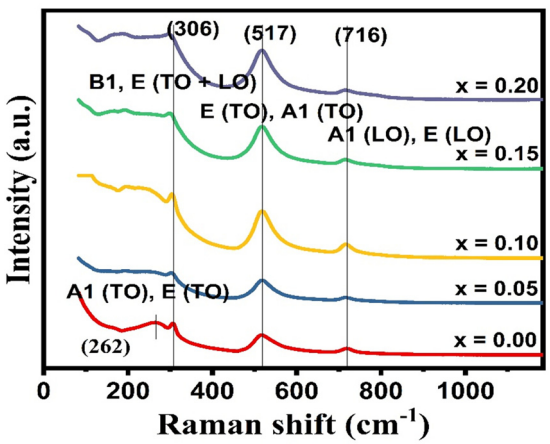

Fig. 3 Raman spectra of $BaZr_xTi_{1-x}O_3$ ceramics (x = 0.00, 0.05, 0.10, 0.15, and 0.20).

3.3. Micro-structural analysis

The FE-SEM images of BZT ceramics with various compositions, x = 0.00, 0.05 0.10 0.15, and 0.20, are displayed in Fig. 4(a)–(e), respectively. The surface morphology and the microstructure of all the samples illustrated in the micrographs showed homogenous morphologies without any chemical contrast among the grains. It could also be observed that the grain boundaries were vibrant, while the full formation of the grain structure indicated that crystals had formed.

The average grain size of each sample was analyzed by imageJ software and the measured sizes are given in Table 2. The average grain size of BT was ~383 nm, with some small pores, as shown in Fig. 4(a). However, the average grain size was decreased substantially because of doping zirconium ions at a certain function of x.

The aggregation of the grains and migration of the grain boundary enabled the BZT sample to develop rapidly in the sintering temperature zone, resulting in greater-sized grains. As a result, defects in the grain growth process were more likely to occur.[29] Fig. 4(c) shows the formation of tiny pores on the surface of the crystal grains. As the Zr content increased, the average grain distribution became more uniform and compact, and the ceramic sample structure became denser, which might have been a result of the liquid-phase sintering effect.

Fig. 5 show the grain-size distribution of each composition for x = 0.00, 0.05, 0.10, 0.15, and 0.20 respectively. After loading Zr ions, the particle size reduction may be the reason for the accumulation of Zr^{4+} to approximately the grain edge, which occurred gradually for the compositions up to x = 0.15. Afterwards, the average grain size increased again for x = 0.20, as shown in Fig. 4(e), may have been due to the coagulation of Zr ions and a mass-transfer process, which was partially responsible for the grain growth during the sintering process.[30]

3.4. Electrical properties

3.4.1. Dielectric constant and dielectric loss tangent. The dielectric constant (ε') of the pure BT and Zr-doped ceramics

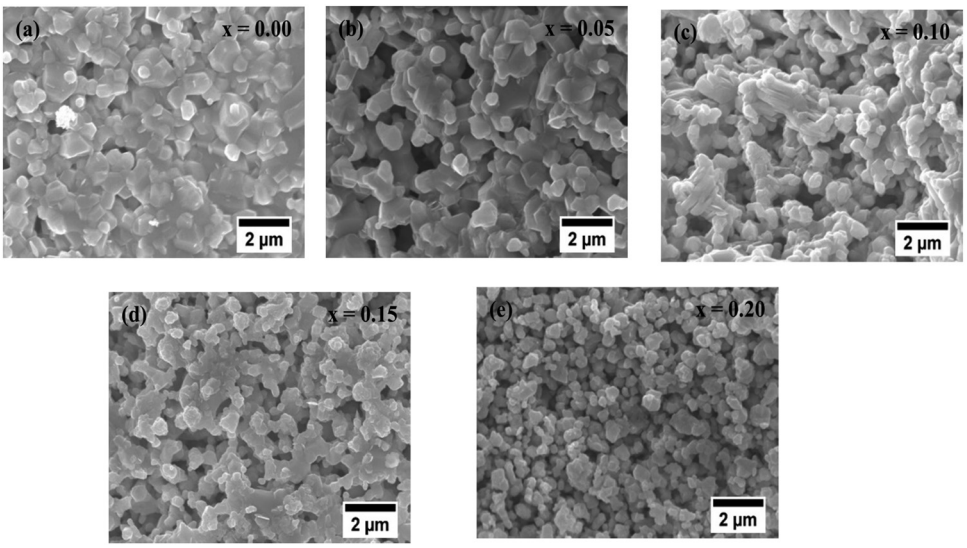

Fig. 4 FE-SEM micrographs of the synthesized BZT ceramics with different compositions: (a) x = 0.00, (b) x = 0.05, (c) x = 0.10, (d) x = 0.15, and (e) x = 0.20.

varied with frequency, as displayed in Fig. 6(a); where ε' was measured at an operating frequency of 40 Hz to 110 MHz. It was observed that ε' showed a general trend of decreasing with increasing frequency in all the samples. This can be explained by the lack of dipoles and the high external alternating frequency of the applied electric field. In addition, the permanent dipoles and the contribution of the charge carriers (ions) of ceramics materials are responsible for decreasing the dielectric constant with increasing the frequency.[30,31]

Fig. 6(b) displays the arcs for the frequency-dependent dielectric loss of the synthesized BZT at room temperature. A high dielectric constant value could be observed at low frequencies, which decreased as the frequency increased for all the synthesized samples. This occurred due to polarization in the dielectric material, which is caused by ionic, dipolar, electronic, and space charge contributions.[32] It is known that a lower frequencies, all forms of polarization play a role in polarization, but as the frequency rises, the influence of the different types of polarization diminishes. At higher frequencies, dipolar and electronic polarization are the main contributors to polarization. Grain boundaries are the only places where space charge accumulation is possible at low frequencies.[33] In addition, the dielectric constant falls as the frequency increases because the space charges are less cable to follow the direction of the field. Only the inherent characteristics of the material will be seen when the space charges fail at a specific high frequency. Thus, it was evident here that the space charge-induced polarization was not effective above 1 MHz frequency and that all the space charges were capable of relaxing.

Moreover, there was a non-polar effect at room temperature, such that ε' also decreased with the doping concentration of zirconium ions (x = 0.05, 0.15, and 0.2), but it showed a maximum increase at x = 0.10, which may have been because of the lower Curie temperature.[31] In the lower frequency range in Fig. 6(a), it can be seen that the value of the dielectric constant was a maximum for the x = 0.10 concentration. However, the dielectric change appeared to be negligible with the increase in frequency and was reduces by only a very small amount. The greater ionic radius pf Zr^{4+} substituted by Ti^{4+} could be affected the arrangement of the B-sites in the oxygen octahedron. This is why, the B–O bond may become weaker, and as a result the phase-transition temperature would drop. The dielectric constant is known to be influenced by the density, tetragonality, and particle size distribution. The difference in grain-size distribution could account for the modest change seen in the dielectric constant.[34] Fig. 6(b) displays the dielectric loss of the examined samples at room temperature, showing that the loss generally decreased at higher frequencies and there was negligible change. Moreover, the larger ionic radius of Zr^{4+} widened the lattice, caused electronic hopping to produce oxygen vacancies, and dielectric loss, thus reducing the conductivity of BZT. It was also observed that the permittivity gradually rose as the Zr content was increased, whereas, the tetragonality declined as the higher zirconium content put more mechanical stress on the structure.[35] This resulted in the formation of oxygen vacancies, porosity, and an irregular structure, thus reducing the dielectric characteristics and increasing the dielectric loss tangent. As seen in Fig. 6(b) $\tan\delta$ experienced a declining trend with increasing frequency.

3.4.2. AC conductivity and impedance. Fig. 7(a) shows the variation of the alternating conductivity (ac) conductivity studied as a function of frequency at room temperature. It was observed that the ac conductivity of the samples was initially unaffected by the applied field, but it increased at high frequency. The continuously rising frequency associated with polarization caused an increase in the electrical conductivity. It was evident that the ac increased upon doping Zr (x = 0.05 to 0.15); however, it decreased for x = 0.20, attributed to the Zr^{4+} substitution, which offered greater chemical stability, reduced

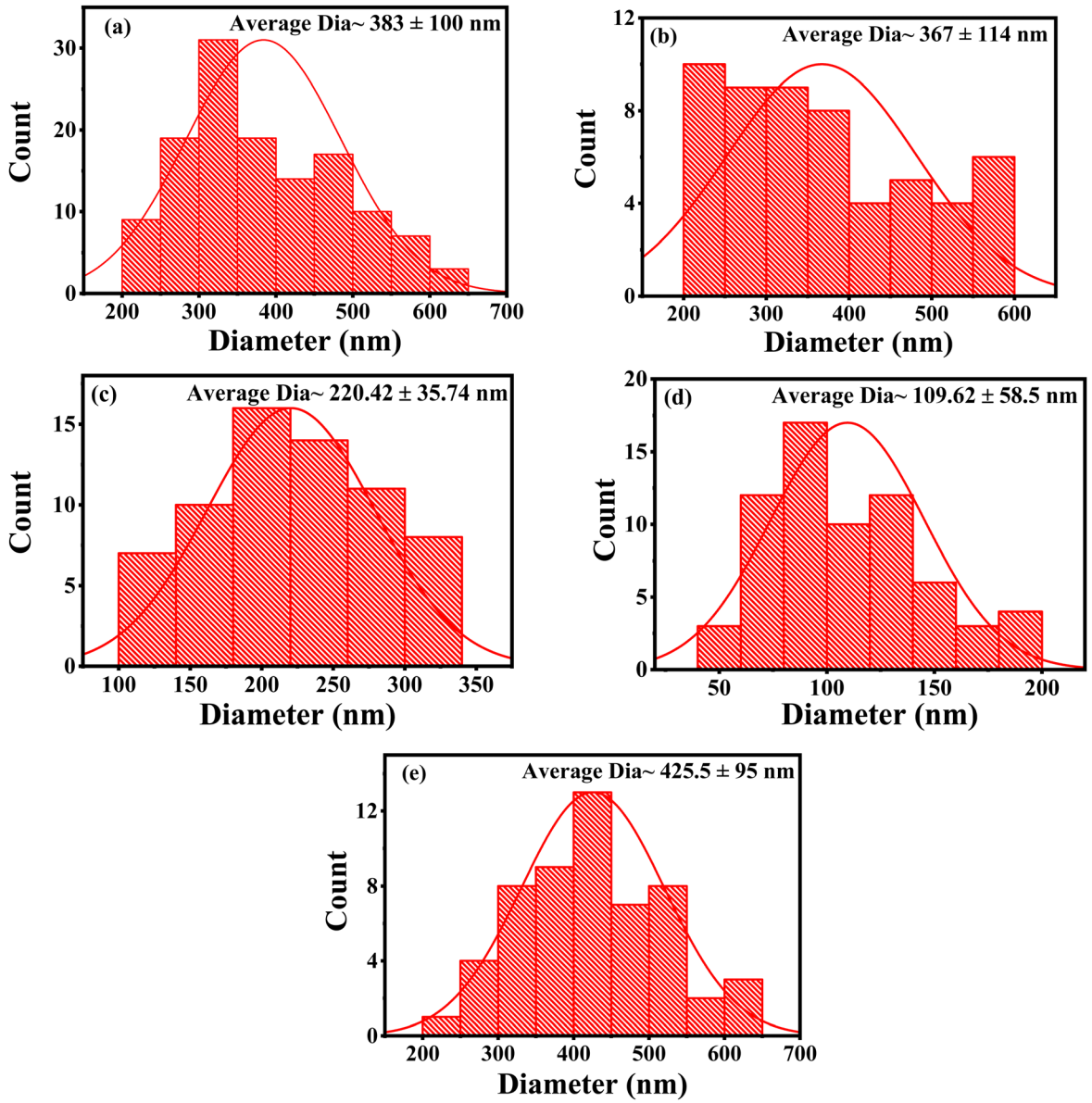

Fig. 5 Grain size distribution of synthesized BZT ceramics with different compositions (a) x = 0.00; (b) x = 0.05; (c) x = 0.10; (d) x = 0.15; and (e) x = 0.20 from FE-SEM images.

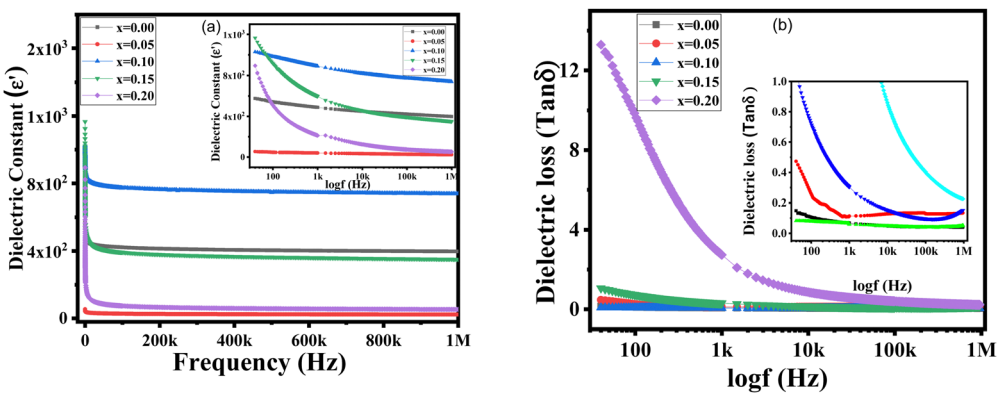

Fig. 6 Frequency-dependent dielectric properties of $BaZr_xTi_{1-x}O_3$ ceramics: (a) dielectric constant; (b) dielectric loss ($\tan\delta$). The inset shows the enlarged view.

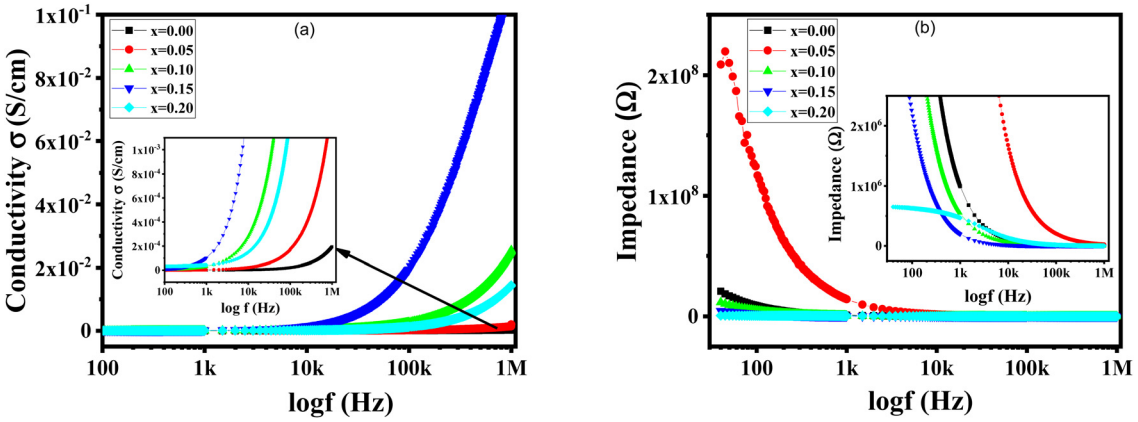

Fig. 7 Frequency *versus* (a) conductivity and (b) impedance of the synthesized BZT samples; insets show magnified views of the respective plots.

the disparity in electron jumping between Ti^{4+} and Ti^{3+}, and increased the resistivity of the materials, resulting in a decrease in the conductivity.[36]

The effect of Zr doping on the real component of impedance varied with the frequency dependency of the BZT samples, as shown in Fig. 7(b). It was observed that the real part of the impedance monotonically declined until the value became constant. The tendency toward merging at higher frequencies, regardless of temperature, was caused through the discharge of the space charge or by the continuous decrease in the barrier characteristics.[25,37]

3.4.3. Piezoelectric analysis. The BZT ceramic showed the piezoelectric effect, meaning if we apply a force to the materials, then charges will be generated on the surface of the materials, so "pC N^{-1}" is used to describe this force to charge the "piezoelectric effect". The piezoelectric coefficient d_{33} is the charge developed on the surface of a piezoelectric material per unit force applied on it. Here the applied force taken was 0.025 N. The d_{33} value was measured for all the synthesized samples and the results are presented in Table 2. The highest value found was 174 for the pC N^{-1} for the x = 0.05 concentration. The value of d_{33} increased with increasing the Zr content, and there was an inverse relationship between the grain size and d_{33}. Because Zr^{4+} has better chemical stability than Ti^{4+}, doping $BaTiO_3$ with Zr^{4+} can enhance the dielectric and piezoelectric characteristics. The piezoelectric properties in ferroelectric materials arise due to electrostatic coupling with spontaneous polarization.[38] As can be seen in Table 2, there was an inverse relationship between the grain size and d_{33}, which was in agreement with ref. 39. The grain size had the most significant impact on the piezoelectric constant; whereby the coupling effect between borders was higher when the grain size increased, producing a drop in domain mobility and polarization, and ultimately a decrease in d_{33}.

3.5. Optical properties

Fig. 8 displays the UV-Vis absorbance spectra of the pure and zirconium-doped BT samples *versus* the incident photons' wavelength. The absorption band was observed in the

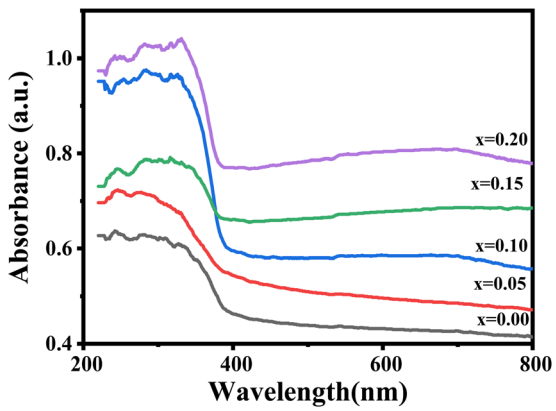

Fig. 8 UV-Vis absorption spectra of $BaTi_{1-x}Zr_xO_3$ ceramics *versus* the wavelength of incident photons.

wavelength range from 220 nm to ~380 nm. Even though all the samples exhibited maximum absorption at approximately 330 nm wavelength, the absorbance increased with the increase in the Zr^{4+} content in the structure, with pure barium titanate achieving the lowest absorption.

The optical band gap energy (E_g) of BT and BZT were measured from the Tauc plot of the UV-Vis-diffuse reflectance spectroscopy data, using the Kubelka–Munk (K–M) approach, which can be denoted by the following formula:[40]

$$F(R_\alpha) = \frac{(1 - R_\alpha)^2}{2R_\alpha}$$

where R_α and $F(R_\alpha)$ are the diffuse reflectance and the function K–M is directly proportional to the absorption coefficient (α). Tauc's law was used to determine the samples' optical band gap energy by permitting an indirect inter band transition between the valence and conduction bands.[38] The optical band gap energy (E_g) of the studied samples was calculated by means of the following Tauc equation:[41]

$$\left[h\nu F(R_\alpha)^{\frac{1}{n}}\right] \propto h\nu - E_g$$

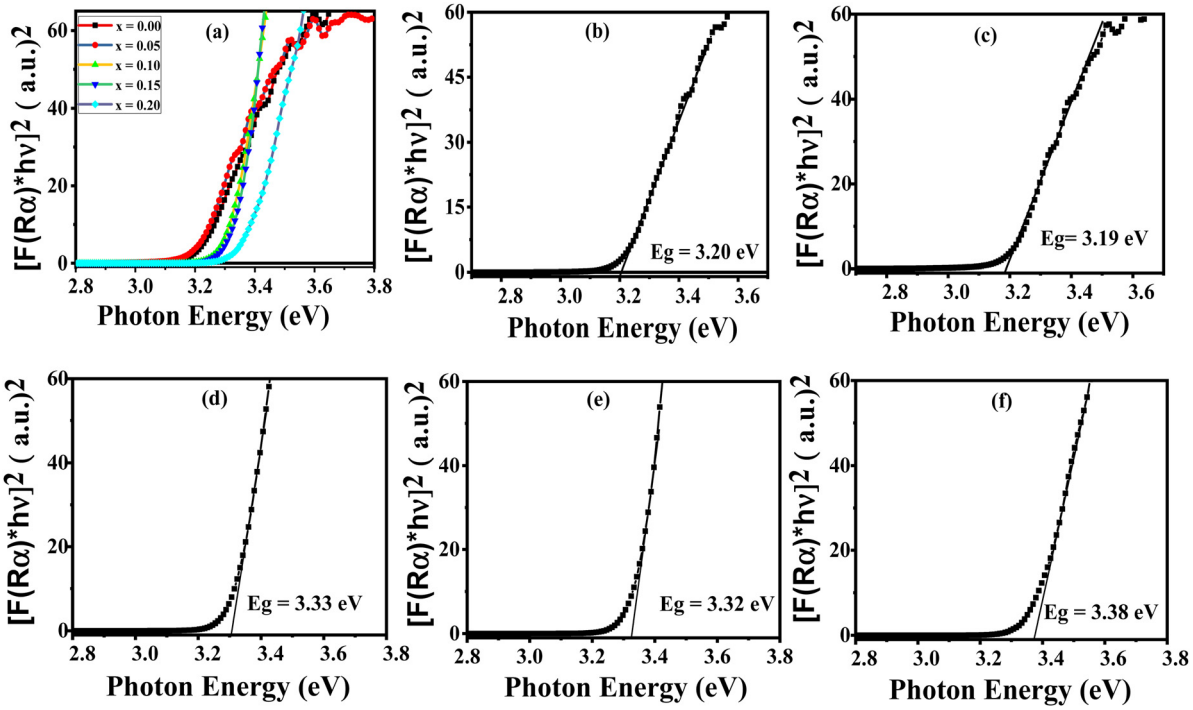

Fig. 9 (a) UV-Visible spectra of BZT powders with different compositions and (b)–(f) Tauc plots for extraction of the optical bandgap from the reflectance data.

where $h\nu$, E_g, and n are the photon energy, band gap energy, and type of band transition, respectively. In this current work, Tauc's plots for the samples were drawn and the results are presented in Table 2.

The band gap energies of BT and BT were evaluated from the intercept of the photon energy axis achieved through extrapolating the plot on the energy axis [photon energy *versus* $(\alpha h\nu)^2$] depicted in Fig. 9. The value of $n = 2$ and $n = 1/2$ were used for the indirect and direct E_g. Fig. 9 shows that the increase in Zr content in the BT structure caused a rise in the band gap energy, except for $x = 0.05$, 3.190 eV, whereby a value of 3.20 eV was attained for pure $BaTiO_3$. The band gap for the $x = 0.05$ sample was shifted to lower energy, which might be a result of the stress induced by the introduction of zirconium into the structure of the barium titanate. The symmetry is broken in the structure owing to the presence of $[ZrO_6]$ clusters.[42] However, for the samples $x = 0.10$, $x = 0.15$, and $x = 0.20$, the E_g values were shifted to higher energies (3.33, 3.32, and 3.38 eV, respectively) compared to pure BT. Increasing the doping concentrations led to an increase in E_g, which may have been caused by a variety of reasons, one of which being the contribution of Zr ions' third orbitals, an increase in interatomic spacing that coincided with the lattice volume growth, or an increase in oxygen vacancies, which in turn would produce an increase in electrons residing in the minimum states near the edge of the conduction band.[43] It is suggested that different factors, such as the crystalline size, structural parameter, and presence of impurities, may responsible for the change in E_g; however, the increase in Eg here may be ascribed to the smaller crystallite size with the increase in Zr^{4+} content in BT.

4. Conclusions

In this research, $BaZr_xTi_{1-x}O_3$ (x = 0.00, 0.05, 0.10, 0.15, and 0.20) materials were successfully synthesized by a solid-state reaction method and the effect of Zr^{4+} doping on the properties of $BaTiO_3$ was investigated. The substitution of Zr^{4+} into the B-sites of $BaTiO_3$ resulted in an increase in the lattice parameters due to the larger ionic radii of Zr^{4+} (0.72 Å) compared to the ionic radii of Ti^{4+} (0.6 Å). In addition, upon Zr doping, the peak at 45.5° was shifted to a lower angle of 45°, owing to tetragonal to cubic structural phase transition. Furthermore, Raman analysis demonstrated that doping resulted in an increase in the line width and a decrease in the magnitudes of the distinctive peaks. The peak at 305 cm^{-1} associated with the tetragonal structure declined, owing to the phase transition from tetragonal to cubic and this was confirmed by the XRD patterns as well. FE-SEM revealed the grains were uniformly distributed and that the grain size decreased until the $x = 0.20$ composition. The dielectric properties were enhanced, and were found to be a maximum for $x = 0.10$. The energy band gap increased with respect to the doping rate. For the sample $BaTi_{0.8}Zr_{0.2}O_3$, the greatest absorption was noted and the band gap energy was improved with increasing the Zr^{4+} ion doping in the prepared perovskite materials, exhibiting an indirect allowed transition. It was also observed that the loss tangent values were relatively minimal while the dielectric constant was rather high. According to the conductivity tests, the sample was primarily insulating. Studies on impedance were effectively used to highlight the conduction mechanism in a sample, and it was determined that the sample was a suitable

dielectric material that can be used in electronic device applications for energy-storage applications, or in multilayer ceramic capacitors.

Data availability

The data supporting this study have been included in the manuscript.

Conflicts of interest

There are no conflicts to declare.

Acknowledgements

Bangladesh Council of Science and Industrial Research (BCSIR), Dr Qudrat-I-Khuda Road, Dhanmondi, Dhaka-1205, Bangladesh and Ministry of Science and Technology, Dhaka, Bangladesh.

References

1 Z. Sun, L. Li, H. Zheng, S. Yu and D. Xu, Effects of sintering temperature on the microstructure and dielectric properties of $BaZr_{0.2}Ti_{0.8}O_3$ ceramics, *Ceram. Int.*, 2015, **41**, 12158–12163, DOI: **10.1016/j.ceramint.2015.06.035**.

2 S. Islam, S. A. Satter, N. Khatun, M. S. Hossain, S. F. U. Farhad, P. Bala, S. Tabassum and A. Siddika, Investigation of Structural, Dielectric and Electrical Properties of Barium Titanate Ceramics Co-Doped with Bismuth and Yttrium, *J. Mol. Eng. Mater.*, 2019, 1–9, DOI: **10.1111/j.1151-2916.1999.tb01921.x**.

3 S. Sharma, K. Shamim, A. Ranjan, R. Rai, P. Kumari and S. Sinha, Impedance and modulus spectroscopy characterization of lead free barium titanate ferroelectric ceramics, *Ceram. Int.*, 2015, **41**, 7713e7722, DOI: **10.1016/j.ceramint.2015.02.102**.

4 R. Ashiri, On the solid-state formation of $BaTiO_3$ nanocrystals from mechanically activated $BaCO_3$ and TiO_2 powders: innovative mechanochemical processing, the mechanism involved, and phase and nanostructure evolutions, *RSC Adv.*, 2016, **6**, 17138, DOI: **10.1039/C5RA22942A**.

5 T. Badapand, V. Senthil, S. Panigrahi and S. Anwar, Diffuse phase transition behavior of dysprosium doped barium titanate ceramic, *J. Electroceram.*, 2013, **31**, 55–60, DOI: **10.1007/s10832-013-9808-x**.

6 S. Yoon, S. Baik, M. G. Kim, N. Shin and I. Kim, Synthesis of tetragonal barium titanate nanoparticles via Alkoxide-Hydroxide sol-precipitation: effect of water addition, *J. Am. Ceram. Soc.*, 2007, **90**, 311e314, DOI: **10.1111/j.1551-2916.2006.01361.x**.

7 J. Q. Qi, T. Peng, Y. M. Hu, L. Sun, Y. Wang, W. P. Chen, L. T. Li, C. W. Nan and H. L. W. Chan, Direct synthesis of ultrafine tetragonal BaTiO3 nanoparticles at room temperature, *Nanoscale Res. Lett.*, 2011, **6**, 466, DOI: **10.1186/1556-276X-6-466**.

8 X. Zhu, J. Zhu, Sh Zhou, Zh Liu and N. Ming, Hydrothermal synthesis of nanocrystalline BaTiO3 particles and structural characterization by high-resolution transmission electron microscopy, *J. Cryst. Growth*, 2008, **310**, 434–441, DOI: **10.1016/j.jcrysgro.2007.10.076**.

9 S. Islam, A. Siddika, N. A. Ahmed, N. Khatun and S. N. Rahman, Synthesis and Characterization of Bismuth doped Barium Titanate, *Am. Int. J. Res. Sci., Technol. Eng. Math.*, 2016, **13**(1), 28–32.

10 K. Yasui, T. Tuziuti and K. Kato, Numerical simulations of sonochemical production of $BaTiO_3$ nanoparticles, *Ultrason. Sonochem.*, 2011, **18**(5), 1211–1217, DOI: **10.1016/j.ultsonch.2011.03.006**.

11 R. Ashiri, Analysis and Characterization of Phase Evolution of Nanosized $BaTiO_3$ Powder Synthesized Through a Chemically Modified Sol–Gel Process, *Metall. Mater. Trans. A*, 2012, **43**, 4414–4426, DOI: **10.1007/s11661-012-1242-1**.

12 Y. Tsur, A. Hitomi, I. Scrymgeour and C. Randall, Site Occupancy of Rare-Earth Cations in $BaTiO_3$, *Jpn. J. Appl. Phys.*, 2001, **40**(1R), 255, DOI: **10.1143/JJAP.40.255**.

13 D.-H. Kuo, C.-H. Wang and W.-P. Tsai, Donor- and acceptor-co substituted $BaTiO_3$ for nonreducible multilayer ceramic capacitors, *Ceram. Int.*, 2006, **32**(1), 1–5, DOI: **10.1016/j.ceramint.2004.11.015**.

14 C. H. Kim, K. J. Park, Y. J. Yoon, M. H. Hong, J. O. Hong and K. H. Hur, Role of Yttrium and Magnesium in the Formation of Core–Shell Struc-ture of $BaTiO_3$ Grains in MLCC, *J. Eur. Ceram. Soc.*, 2008, **28**(6), 1213–1219, DOI: **10.1016/j.jeurceramsoc.2007.09.042**.

15 Q. Xu and Z. Li, Dielectric and ferroelectric behavior of Zr-doped $BaTiO_3$ perovskites, *Process. Appl. Ceram*, 2020, **14**(3), 188–194, DOI: **10.2298/PAC2003188X**.

16 B. W. Ricketts, G. Triani and A. D. Hilton, Dielectric energy storage densities in $Ba_{1-x}Sr_xTi_{1-y}Zr_yO_3$ ceramics, *J. Mater. Sci. Mater. Electron.*, 2000, **11**, 513–517, DOI: **10.1023/A:1008924703491**.

17 P. Julphunthong, S. Chootin and T. Bongkarn, Phase formation and electrical properties of $Ba(Zr_xTi_{1-x})O_3$ ceramics synthesized through a novel combustion technique, *Ceram. Int.*, 2013, **39**(1), S415–S419, DOI: **10.1016/j.ceramint.2012.10.105**.

18 S. Islam, A. Siddika, N. A. Ahmed, N. Khatun and S. N. Rahman, Structural, Dielectric and Electric Properties of Manganese-Doped Barium Titanate, *Int. J. Nanoelectron. Mater.*, 2018, **11**, 419–426.

19 A. Mandal, D. Yadav, S. K. Mittal, U. Jamwal, D. Kaneria, A. Khokhar, M. Jakhar and K. L. Yadav, Investigation of structural, morphological, dielectric, optical, and ferroelectric-energy storage properties of $[(1-x)BCT_{-(x)}BZT]$ electroceramics, *J. Alloys Compd.*, 2024, **995**, 174817, DOI: **10.1016/j.jallcom.2024.174817**.

20 E. H. Yahakoub, A. Bendahhou, K. Chourti, F. Chaou, I. Jalafi, S. E. Barkany, Z. Bahari and M. A. Salama, Structural, electrical, and dielectric study of the influence of 3.4% lanthanide (Ln^{3+} = Sm^{3+} and La^{3+}) insertion in the A-site of perovskite $Ba_{0.9}5Ln_{0.034}Ti_{0.99}Zr_{0.01}O_3$, *RSC Adv.*, 2022, **12**, 33124, DOI: **10.1039/d2ra06758g**.

21 V. S. Puil, D. K. Pradhan, B. C. Riggs, S. Adireddy, R. S. Katiyar and D. B. Chrisey, Synthesis and characterization of lead-free ternary component BST-BCT-BZT ceramic capacitor, *J. Adv. Dielectr.*, 2014, **4**(2), 14500143, DOI: 10.1142/S2010135X14500143.

22 S. Islam, N. Khatun, M. S. Habib, S. F. U. Farhad, N. I. Tanvir, M. A. A. Shaikh, S. Tabassum, D. Islam, M. S. Hossain and A. Siddika, Effects of yttrium doping on structural, electrical and optical properties of barium titanate ceramics, *Heliyon*, 2022, **8**(9), E10529, DOI: 10.1016/j.heliyon.2022e10529.

23 E. Hannachi, M. A. Almessiere, Y. Slimani, R. B. Alshamrani, G. Yasin and F. Ben Azzouz, Preparation and characterization of High-T_c $(YBa_2Cu_3O_{7-\delta})_{1-x}/(CNTs)_x$ superconductors with highly boosted superconducting performances, *Ceram. Int.*, 2020, **47**(16), 23539–23548, DOI: 10.1016/j.ceramint.2021.05.071.

24 A. Nfissi, Y. Ababou, M. Belhajji, S. Sayouri and T. Lamcharfi, Structural and dielectric properties of sol–gel processed Ce-doped $BaTi_{0.9}7Y_{0.03}O_3$ ceramics, *J. Adv. Dielectr.*, 2021, **11**(1), 2150003, DOI: 10.1142/S2010135X2150003X.

25 P. Arpita and K. Rajesh Kumar, Hafnium (Hf) doped $BaTiO_3$: A study of structural and electrical properties for device application feasibility, *Int. J. Novel Res. Dev.*, 2024, **9**(4), b604–b616.

26 H. Z. Akbas, Z. Aydin, F. Guder and S. Turgut, Accelerated formation of $BaTiO_3$ ceramics with mechano-chemical processing in different liquids, *J. Alloys Compd.*, 2017, **699**, 87e91, DOI: 10.1016/j.jallcom.2016.12.369.

27 N. K. Karan, R. S. Katiyar, T. Maiti, R. Guo and A. S. Bhalla, Raman spectral studies of Zr^{4+}-rich $BaZr_xTi_{1-x}O_3$ $(0.5 \leq x \leq 1.00)$ phase diagram, *J. Raman Spectrosc.*, 2009, **40**(4), 370–375, DOI: 10.1002/jrs.2134.

28 A. El ghandouri, S. Sayouri, T. Lamcharfi and L. Hajji, Effect of strontium on the structural and piezoelectric properties of the sol gel processed barium titanate, *J. Mater. Environ. Sci.*, 2017, **8**(S), 4945–4962.

29 C. Q. Wang, C. Shu and D. Y. Zheng, *et al.*, Effects of Li and Y co-doping on electrical properties and dielectric relaxation behavior of BCZT ceramics, *J. Mater. Sci.: Mater. Electron.*, 2022, **33**, 3822–3834, DOI: 10.1007/s10854-021-07573-z.

30 K. Xi, Y. Li, Z. Zheng, L. Zhang, Y. Liu and Y. Mi, Microstructure, dielectric properties, relaxation behavior, and ferroelectric properties of Gd-doped lead-free BZT ceramics by sol–gel process, *J. Mater. Sci.: Mater. Electron.*, 2020, **24**, 23044–23051, DOI: 10.1007/s10854-020-04832-3.

31 M. Graca, M. A. Valente and M. G. Ferreira da Silva, Electrical properties of lithium niobium silicate glasses, *J. Non-Cryst. Solids*, 2003, **325**(1–3), 267–274, DOI: 10.1016/S0022-3093(03)00314-4.

32 P. Bergo, W. M. Pontuschka and J. M. Prison, Dielectric properties of P_2O_5-Ni_2O–Li_2 glasses containing WO_3, CoO or Fe_2O_3, *Solid State Commun.*, 2007, **141**(10), 545–547, DOI: 10.1016/j.ssc.2006.12.024.

33 R. Tomar, R. Pandey, N. B. Singh, M. Kumar Gupta and P. Gupta, Electrical properties of barium titanate in presence of Sn^{2+} dopant, *SN Appl. Sci.*, 2020, **2**, 226, DOI: 10.1007/s42452-020-2017-8.

34 N. Gouitaa, L. Taj-Dine, A. Farid and A. Fatima Zahra, Structural, Dielectric and Electrical Properties of Modified $BaTi_{0.80}Fe_{0.20}O_3$ Ceramics by Zr Addition in Ti Site at X = 0.00 to 0.10, *Iran. J. Mater. Sci. Eng.*, 2021, **18**(3), 1–12.

35 L. Xu and Y. Xu, Effect of Zr^{4+} content on crystal structure, micromorphology, ferroelectric and dielectric properties of $Ba(Zr_xTi_{1-x})$ O_3 ceramics, *J. Mater. Sci.: Mater. Electron.*, 2020, **31**, 5492–5498, DOI: 10.1007/s10854-020-03114-2.

36 I. Ullah, M. Ur Rehman, A. Manan, M. T. Lanagan, R. Wali Khan, A. Ullah, S. Wali Ullah and M. Uzair, Structural, dielectric, electrical, and energy storage properties of Mn-doped $Ba_{0.55}Sr_{0.45}TiO_3$ ceramic, *Int. J. Appl. Ceram. Technol.*, 2024, **21**(5), 1–9, DOI: 10.1111/ijac.14788.

37 S. Mahajan, O. P. Thakur, P. Chandra and K. Sreenivas, Effect of Zr on dielectric, ferroelectric and impedance properties of $BaTiO_3$ ceramic, *Bull. Mater. Sci.*, 2011, **34**, 1483–1489, DOI: 10.1007/s12034-011-0347-2.

38 T. Badapanda, S. Sarangi, B. Behera, S. Anwar, T. P. Sinha, R. Ranjan, G. E. Luz Jr., E. Longo and L. S. Cavalcante, Structural refinement, optical and electrical properties of $[Ba_{1-x}Sm_{2x}/3]$ $(Zr_{0.05}Ti_{0.95})O_3$ ceramics, *J. Mater. Sci.: Mater. Electron.*, 2014, **25**, 3427–3439, DOI: 10.1007/s10854-014-2035-7.

39 M. M. Salem, M. A. Darwish, A. M. Altarawneh and Y. A. Alibwaini, *et al.*, Investigation of the structure and dielectric properties of doped barium titanates, *RSC Adv.*, 2024, **14**, 3335–3345, DOI: 10.1039/D3RA05885A.

40 N. Khatun, S. Ahmed, M. S. Hossain, S. F. U. Farhad, M. A. Mamun, M. S. Alam, M. H. A. Begum, N. I. Tanvir, M. Hakim and S. Islam, Influence of $Y^{3+}$and La^{3+} ions on the structural, magnetic, electrical, and optical properties of cobalt ferrite nanoparticles, *Heliyon*, 2023, **9**, e13019, DOI: 10.1016/j.heliyon.2023.e13019.

41 T. Chen, J. Meng, S. Wu, J. Pei, Q. Lin, J. Wei, X. Wei, J. Li and Z. Zhang, Room temperature synthesized $BaTiO_3$ for photocatalytic hydrogen evolution, *J. Alloys Compd.*, 2018, **754**, 184, DOI: 10.1016/j.jallcom.2018.04.300.

42 L. S. Cavalcante, V. M. Longo, M. Zampieri, J. W. M. Espinosa, P. S. Pizani, J. R. Sambrano, J. A. Varela, E. Longo, M. L. Simões and C. A. Paskocimas, Experimental and theoretical correlation of very intense visible green photoluminescence in $BaZrO_3$ powders, *J. Appl. Phys.*, 2008, **103**, 063527.

43 M. Reda, E. E. Ateia, S. I. El-Dek and M. M. Arman, New insights into optical properties, and applications of Zr-doped $BaTiO_3$, *Appl. Phys. A: Mater. Sci. Process.*, 2024, **130**, 240, DOI: 10.1007/s00339-024-07381-2.